

RESEARCH ARTICLE

The aerodynamics of flying snake airfoils in tandem configuration

Farid Jafari^{1,*}, Daniel Holden², Roderick LaFoy², Pavlos P. Vlachos³ and John J. Socha⁴

ABSTRACT

Flying snakes flatten their body to form a roughly triangular cross-sectional shape, enabling lift production and horizontal acceleration. While gliding, they also assume an S-shaped posture, which could promote aerodynamic interactions between the fore and the aft body. Such interactions have been studied experimentally; however, very coarse models of the snake's cross-sectional shape were used, and the effects were measured only for the downstream model. In this study, the aerodynamic interactions resulting from the snake's posture were approximated using two-dimensional anatomically accurate airfoils positioned in tandem to mimic the snake's geometry during flight. Load cells were used to measure the lift and drag forces, and flow field data were obtained using digital particle image velocimetry (DPIV). The results showed a strong dependence of the aerodynamic performance on the tandem arrangement, with the lift coefficients being generally more influenced than the drag coefficients. Flow field data revealed that the tandem arrangement modified the separated flow and the wake size, and enhanced the lift in cases in which the wake vortices formed closer to the models, producing suction on the dorsal surface. The downforce created by the flow separation from the ventral surface of the models at 0 deg angle of attack was another significant factor contributing to lift production. A number of cases showing large variations of aerodynamic performance included configurations close to the most probable posture of airborne flying snakes, suggesting that small postural variations could be used to control the glide trajectory.

KEY WORDS: Gliding, Biomechanics, Tandem airfoils, *Chrysopelea*, Particle image velocimetry

INTRODUCTION

Snakes in the Southeast Asian genus *Chrysopelea* have evolved the ability to glide (Socha, 2002, 2011; Socha et al., 2015). As they lack specialized surfaces to produce aerodynamic forces, they instead use their entire body as a wing. Once airborne, the snake splays its ribs to transform a rounded cylindrical body to a roughly triangular cross-sectional shape (Fig. 1A), which has the effect of increasing the projected area and lowering the profile in the dorsoventral axis. In addition to this body flattening, flying snakes undulate laterally by sending traveling waves posteriorly down the body. At any instant, the snake appears to assume an S-like posture (Fig. 1B), but the undulating motion continuously repositions the body, with substantial displacement in the vertical axis (Fig. 1C). As the snake

moves through its glide trajectory, its glide path shallows, and the relative orientation of the oncoming airflow changes accordingly. Although the body can be considered as a single, reconfigurable wing, it can also be viewed as a composite of many segments, whose specific orientation and positioning relative to the airflow varies throughout the glide. In certain configurations, downstream segments may interact with the wake created by upstream segments. How does this continuous repositioning of the body during aerial undulation influence the snake's aerodynamics?

The cross-sectional shape of the body plays a major role in the snake's glide performance. In *Chrysopelea paradisi*, this shape is symmetrical in the fore–aft axis, with a semi-triangular dorsal surface, a flat ventral surface, and a pair of ventrally oriented ‘lips’ on each lateral edge (Socha, 2011) that appear to run along most of the length of the body between the snout and vent, producing a concave shape. Although this cross-section can be modeled as a bluff body, its aerodynamic performance is superior to some airfoils in steady flows at similar Reynolds numbers (Holden et al., 2014). Two studies provide our current understanding of the aerodynamics of this two-dimensional shape (Holden et al., 2014; Krishnan et al., 2014). Positive lift is created at angles of attack (α) greater than 10 deg, with lift coefficients ranging from approximately 1.0 to 1.5 at Reynold numbers between 3000 and 15,000. The lift coefficient tends to be slightly higher at lower Reynolds numbers within this range. Lift coefficients peak sharply at $\alpha=35$ deg and gradually decrease up to the maximum studied angle of 60 deg. Drag coefficients also increase dramatically after $\alpha=35$ deg. Vortex trajectory analysis of the experimental velocity field and subsequent computational investigations (Krishnan et al., 2014) suggest that vortex-induced suction on the dorsal surface of the snake may underlie the surprisingly high lift coefficients at 35 deg. Overall, near-maximum lift-to-drag ratios (L/D) ranging from 1.3 to 2.7 occur between $\alpha=15$ deg and $\alpha=40$ deg, and positive L/D occurs beyond $\alpha=10$ deg, providing a physical rationale for the snake's glide performance.

However, the aerodynamic performance of single two-dimensional airfoils alone is not sufficient to explain the gliding abilities of real snakes. For instance, the shallowest glide angle reported for *C. paradisi*, 13 deg (Socha et al., 2005), indicates that flying snakes are capable of achieving an average L/D of 4.5, which is almost twice as large as the maximum value of 2.7 found in the modeling study by Holden et al. (2014). As first-order approximations, initial studies neglected a range of complexities of the system, including undulation, 3D shape, possible variation of the snake profile along the body, and unsteady effects. Clearly, some aerodynamic mechanisms that contribute to glide performance remain unexplained. Unsteady and 3D effects have previously been shown to augment lift in some biological systems (e.g. Bahlman et al., 2013; Wang et al., 2014; Shyy et al., 2009; Song et al., 2014; Muijres et al., 2008; Lentink and Dickinson, 2009; Bompfrey et al., 2006), but the snake's large advance ratio (the ratio of the forward motion to the reciprocating motion) compared with that of insects and birds (Vogel, 2003; Dickson and Dickinson, 2004; Holden et al., 2014) suggests that unsteady mechanisms are less likely

¹School of Engineering, Grand Valley State University, Grand Rapids, MI 49504, USA. ²Department of Mechanical Engineering, Virginia Tech, Blacksburg, VA 24060, USA. ³Department of Mechanical Engineering, Purdue University, West Lafayette, IN 47906, USA. ⁴Department of Biomedical Engineering and Mechanics, Virginia Tech, Blacksburg, VA 24061, USA.

*Author for correspondence (jafari@gvsu.edu)

© F.J., 0000-0003-3252-5111; J.J.S., 0000-0002-4465-1097

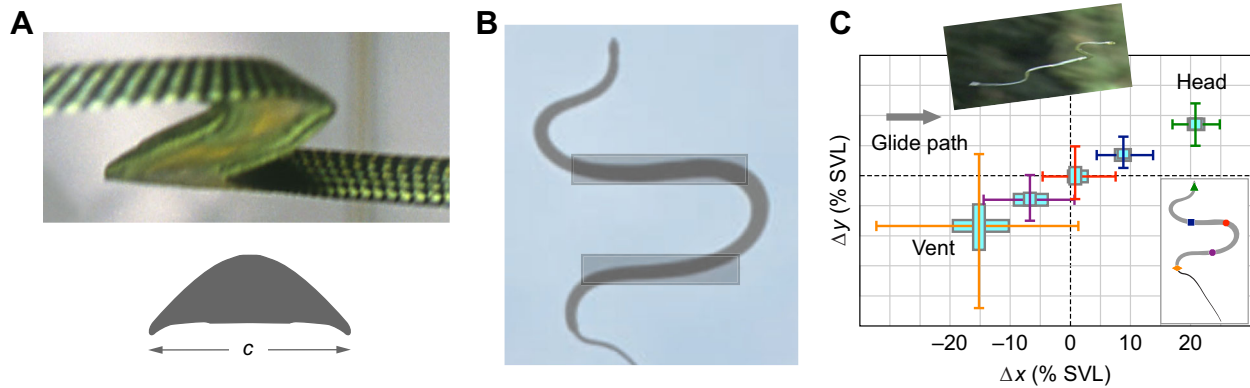


Fig. 1. The flying snake body shape and posture while airborne. (A) The snake flattens its body when airborne, creating an unconventional airfoil to produce lift (adapted from Socha, 2011). c , chord length (B) The snake assumes an S-like posture, in which the body parts that are roughly perpendicular to the airflow can be considered as a pair of airfoils in tandem. (C) During the developed stage of glide, the snake maintains a staggered posture, as evidenced by the experimental kinematic data from *Chrysopelea paradisi*. The data shown summarize the displacement of five landmarks on the snake body relative to its center of mass and normalized with respect to the snout–vent length (SVL) (adapted from Socha et al., 2010).

to produce a significant aerodynamic contribution. Recent studies (Jafari et al., 2017; Yeaton et al., 2020) found that undulation does have a functional influence on glide performance, acting to increase the stability of the snake. However, the theoretical modeling of the snake only incorporated single-foil aerodynamic coefficients, and did not examine interactive aerodynamics.

Here, we focused on the aerodynamic effects of the relative positioning and orientation of the body. Specifically, we hypothesized that the staggered S-shaped configuration of the gliding snake produces a complex interaction between the fore and aft body segments, whereby wake formed upstream is intercepted by downstream segments. Such tandem interactions have been observed in flapping wings (particularly in dragonflies) with an often favorable contribution to the aerodynamics (Akhtar et al., 2007; Lehmann, 2008, 2009; Maybury and Lehmann, 2004; Usherwood and Lehmann, 2008; Wang and Russell, 2007; Warkentin and DeLaurier, 2007; Weimerskirch et al., 2001). Static tandem airfoils (with $Re \approx 10^4$ – 10^5) have been shown to experience mixed aerodynamic effects (Scharpf and Mueller, 1992; Michelsen and Mueller, 1987; Husain et al., 2005), demonstrating that tandem arrangements can also produce poorer performance. A preliminary study by Miklasz et al. (2010) on flying snakes suggested that tandem effects may be substantial in certain configurations. They found that certain configurations of gap (defined as the horizontal spacing difference) and stagger (defined as the vertical spacing difference) resulted in changes in L/D relative to a single airfoil, increasing as much as $\sim 50\%$ and decreasing by $\sim 20\%$. However, that study used simple models that lacked an anatomically accurate shape, kept the angles of attack fixed at a single value (of 25 deg), measured forces only on one airfoil, and only explored a small portion of the gap–stagger parameter space.

In this study, we used anatomically accurate 3D-printed models to examine the interactions of two flying snake airfoils, representing upstream and downstream body segments. The angles of attack and the gap and stagger between the two airfoils were varied to reproduce a wide range of conditions experienced by the snake during aerial undulation. Load cells were used to measure the individual lift and drag forces acting on each airfoil, and in follow-up trials, digital particle image velocimetry (DPIV) provided flow fields to examine configurations of particular interest. By determining the physical bounds on the aerodynamic capabilities of the tandem airfoils, this study furthers our

knowledge about how flying snakes produce forces for gliding and control, and allows us to predict the limits on the snake's aerial performance.

MATERIALS AND METHODS

First, load cells were used to measure the lift and drag forces on each of the airfoils in the tandem arrangement. Next, we used DPIV to obtain the flow field measurements for select cases that exhibited significant lift enhancement compared with single airfoil models. The velocity field results were used to estimate the aerodynamic forces and verify the load cell measurements, to look at the dynamical interactions between the fore and aft sections, and to investigate the specific sources of the high lift coefficients.

Experiment test matrix

In designing our experiments, we aimed to minimize the number of independent variables so that the number of test cases would not become impractically large. Previous measurements (Holden et al., 2014) showed that the aerodynamic performance of a single airfoil is only mildly dependent on the Reynolds number. So, we kept the Reynolds number constant at $Re = 13,000$, which corresponds to an adult snake in a fully developed glide (Socha et al., 2005). We addressed the effects of variation in spacing (gap and stagger) between the airfoil sections of the snake, and the airfoil's angle of attack. Thus, the parameter space consisted of the distance between the airfoils parallel to the flow (gap, Δx), the distance perpendicular to the flow (stagger, Δy), and the upstream and downstream angles of attack, α_u and α_d . Sampling of this large parameter space entailed a trade-off between being able to capture the important physical phenomena and generating a feasible test matrix. To reduce the volume of the parameter space, we focused on the set of parameters that are most typical of snakes during flight based on the previously determined kinematic data (Socha et al., 2010). Guided by these data, the gap and stagger distances were varied over the ranges $2c < \Delta x < 8c$ (with increments of $2c$) and $0c < \Delta y < 5c$ (with increments of $1c$), where c is the chord length of the airfoil. As no data exist on the snake's exact angles of attack along the body, we used the range of glide angles across the whole body reported in Socha et al. (2005) as the basis for the range of angles of attack in the experiments: $0 \leq \alpha_u, \alpha_d \leq 60$ deg. This approximation is justified by the kinematic data indicating that the snakes glide with the ventral portion of the

Table 1. The test matrix for the load cell measurements

Δx (c)	Δy (c)	(α_u, α_d)
2	0	(30 deg, 0 deg)
4	1	(30 deg, 20 deg)
6	2	(30 deg, 40 deg)
8	3	(30 deg, 60 deg)
	4	(0 deg, 30 deg)
	5	(20 deg, 30 deg)
		(40 deg, 30 deg)
		(60 deg, 30 deg)

Δx , gap (the distance between airfoil sections parallel to the flow); Δy , stagger (the distance between airfoil sections perpendicular to the flow); c , chord length of the airfoil; α_u and α_d , upstream and downstream angles of attack. Table entries, one from each column, were combined to determine the test points in the parameter space. Overall, there were $4 \times 6 \times 8 = 192$ combinations.

body facing the ground (Socha et al., 2010). This means that typically the body cross-sectional shape is approximately aligned with the plane of mean body posture. We also considered the possibility that the fore and the aft body may not have the same angle of attack, but we assumed that the snake cannot exhibit extreme values of twist (Moon, 1999); therefore, we rejected combinations with difference of greater than 30 deg between α_u and α_d . The test matrix with a total of 192 ($=4 \times 6 \times 8$) trials is summarized in Table 1. The combinations of the angles of attack were sorted in two groups: (i) the upstream angle of attack was kept fixed at $\alpha_u = 30$ deg and the downstream angle of attack was varied from $\alpha_d = 0$ deg to 60 deg, and (ii) the downstream angle of attack was kept fixed at $\alpha_d = 30$ deg and the upstream angle of attack was varied from $\alpha_u = 0$ deg to 60 deg.

Experimental setup

All experiments were conducted with models that were geometrically accurate replicas of the cross-sectional shape of the airborne snake (Fig. 1A). Each model was fabricated in a stiff acrylate photopolymer (VeroWhite, Sculpteo, San Leandro, CA, USA) using a material-jetting additive manufacturing system (Connex 350, Stratasys, Eden Prairie, MN, USA). The models had a chord width of 25.4 mm and an aspect ratio of 20 to simulate the approximately straight sections of the snake's body normal to the flow (Fig. 1B). The models spanned the entire width of the tunnel to eliminate end effects, as in Holden et al. (2014). The experiments were conducted in a closed-loop water tunnel at Virginia Tech with a $0.6 \times 0.6 \times 1.5$ m test section. The freestream turbulence intensity at the test location was less than 3% at speeds up to 0.5 m s^{-1} (Gifford et al., 2011). The speeds were chosen to maintain Reynolds number similarity to the range exhibited by the snakes in the air (Socha, 2011).

The experimental setup was a modified version of the one used in Holden et al. (2014). Two grids of holes were drilled in the sidewalls to accommodate the second model, either upstream or downstream from the first (Fig. 2A). With this configuration, the forces on one of the models were measured while the other model was fixed to the sidewalls. Four 5 lb (22 N) load cells (LCFD-5, accuracy: $\pm 0.15\%$ FSO, DMD-465WB, strain-gage amplifiers; Omega Engineering, Stamford, CT, USA) were used to simultaneously measure the vertical and horizontal forces on the model. LabVIEW software (National Instruments, Austin, TX, USA) and a DAQ board (NI PCI-6251) were used to record the data for each trial at a sampling rate of 1000 Hz for 30 s. The weight of the experimental setup and model was accounted for by zeroing the force measurement before each trial.

The lift and drag coefficients were calculated as:

$$C_L = \frac{2F_L}{\rho U^2 c l}, \quad (1a)$$

$$C_D = \frac{2F_D}{\rho U^2 c l}, \quad (1b)$$

where F_L and F_D are the measured lift and drag forces, ρ is the water density, U is the freestream velocity, c is the chord length, and l is the span length of the model. The uncertainty in these calculations was evaluated using the law of propagation of uncertainty with the same method as in Holden (2011).

Flow field measurements

The flow field was spatiotemporally resolved using planar DPIV measurements. To minimize the undesirable optical effects in the captured images, the acrylic sidewalls of the force-measuring setup were modified to accommodate detachable walls of acrylic specifically cut for each combination of gap and stagger (Fig. 2B). The experimental models were rigidly mounted to the detachable walls for the DPIV measurements. To seed the water tunnel, small, neutrally buoyant, hollow glass spheres (mean diameter, $126.4 \mu\text{m}$; Potters Industries, Valley Forge, PA, USA) were used to act as flow tracers. The particles were illuminated using a dual-head laser system (Pegasus PIV, New Wave Research, Portland, OR, USA). Optical elements were used to spread the laser beam into a thin sheet with an approximately 1 mm thickness. To eliminate the shadow cast by the models, two mirrors were placed in a windowed box submerged into the water above the experimental setup to reflect the laser plane back through the test section. The desired region of interest included the two models, the distances between them (maximum of 6 chords of gap and 3 chords of stagger; Table 1), and the downstream wake. We used two cameras to capture this large region with sufficient resolution, including adequate overlap between the field of view of the two cameras. To capture the entire height of the desired field of view, the cameras were placed at one chord length vertical offset for the cases with stagger of $\Delta y = 2c$ or $3c$, and at the same level for the cases with stagger of $\Delta y = 0c$ or $1c$ (Fig. 2C). High-speed video cameras (XS-5, Integrated Design Tools, Tallahassee, FL, USA) were used to record 1024×1280 pixel images at a sampling rate of 1000 Hz. Using 105 mm lenses with an aperture of $f/2.0$, an average image magnification of $108.1 \mu\text{m}/\text{pixel}$ was achieved. Before taking each set of data, a calibration grid (an aluminium plate with a grid of 3.2 mm dots at 12.7 mm spacing) was placed at the laser sheet plane and recorded. The calibration data were used to correctly overlap and align the images of the two cameras.

The time-resolved DPIV images were processed with the publicly available code PRANA (Eckstein and Vlachos, 2009a,b; Eckstein et al., 2008). We used the Robust Phase Correlation (RPC) algorithm with three iterations of multigrid iterative deformable windows (Scarano, 2001) to correlate the images and determine the instantaneous velocity fields. A window deformation algorithm was used as it is known to produce higher accuracy velocity field measurements by preventing the loss of particle-image pairs as the result of in-plane shear (Scarano and Riethmuller, 2000). Gaussian image masking was applied to the image windows to decrease induced high-frequency noise in the cross-correlations. Between passes, spatial filtering of the velocity fields was used to stabilize the iterative process (Schrijer and Scarano, 2008). The DPIV processing was carried out with three passes, one pass with 64×64 pixel interrogation windows, and two passes with 32×32 pixel interrogation windows. After each pass, the results were validated

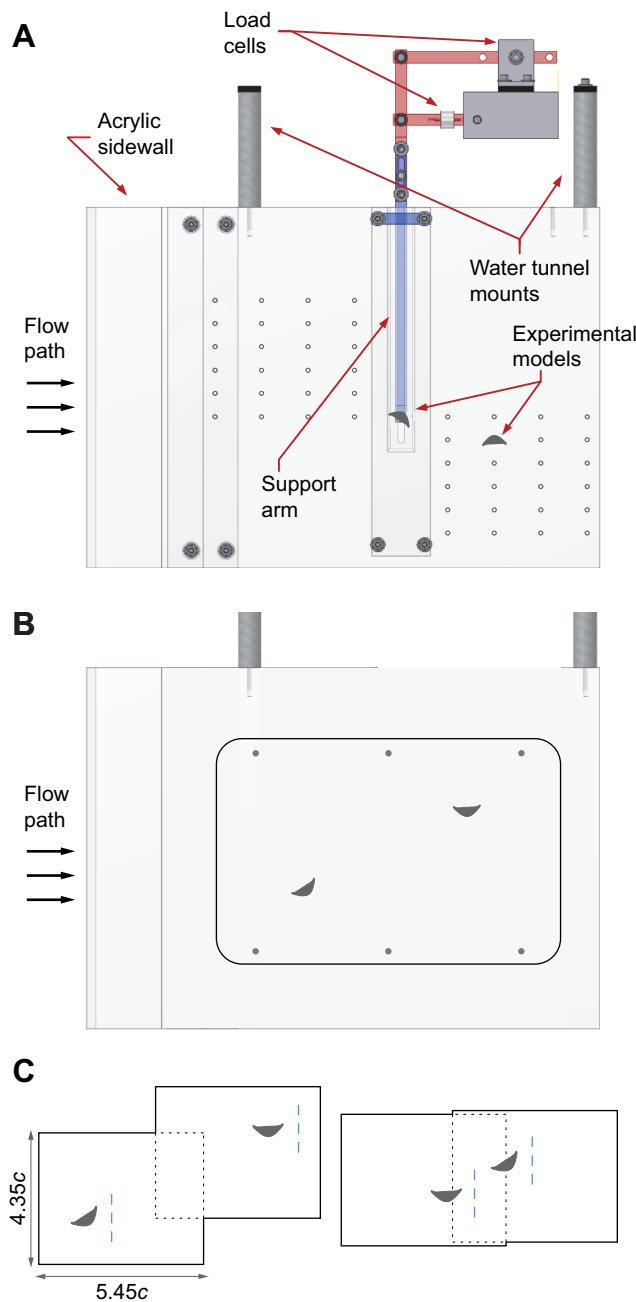


Fig. 2. Force and digital particle image velocimetry (DPIV) measurement setup. (A) The sidewalls of the setup used to measure forces on a single airfoil were modified with two grids of holes to accommodate a second model. With the new setup, measurements could be done on one of the airfoils, while the other one was fixed to the walls. (B) The sidewalls of the force measurement setup were modified to accommodate acrylic plates designed for each combination of gap and stagger. The airfoils were fixed to the plates upside down to minimize the shadows. This setup was used for DPIV measurements. (C) Two cameras were needed to capture the full field of view encompassing both models. For two or three chords of stagger, the cameras were placed with one chord length of vertical offset, whereas they were placed level for smaller staggers. The blue dashed lines indicate the position where power spectral analysis was performed on the velocity data.

using velocity thresholding and universal outlier detection to replace vectors calculated from incorrectly matched correlation peaks (Westerweel and Scarano, 2005). The final processed velocity fields had a uniform vector grid spacing of 8 pixels.

Analysis of the data

Spectral analysis was performed on the force coefficients (Eqns 1a and 1b) to determine the dominant spectral components and vortex shedding behavior. The frequencies were non-dimensionalized using:

$$f^* = \frac{fh}{U}, \quad (2)$$

where f is the temporal frequency, h is the characteristic length, and U is the freestream velocity. The characteristic length was considered for both models to be the same and equal to the projection of the model with 30 deg angle of attack perpendicular to the freestream. Spectral analysis also was performed on the velocity field, one chord length downstream of the centroid of each airfoil (Fig. 2C).

Next, we used proper orthogonal decomposition (POD) with the method of snapshots (Smith et al., 2005; Berkooz et al., 1993) to decompose the dataset into orthogonal basis functions that capture the energetically important modes of the data. As the lower energy modes were more likely to be overwhelmed by experimental noise, the influences from the noise could be minimized by removing those modes (Charonko et al., 2010). Here, we reconstructed the velocity field by keeping the modes that accounted for 80% of the total energy.

The force acting on each airfoil was calculated from the filtered velocity field using the integral form of the momentum equation for a steady control volume surrounding the airfoil:

$$\bar{F} = - \iiint_V \rho \frac{\partial \bar{v}}{\partial t} dV - \oint_S \rho \bar{v} (\bar{v} \cdot \hat{n}) dS - \oint_S p \hat{n} dS + \oint_S \hat{n} \cdot \bar{\tau} dS, \quad (3)$$

where \bar{F} is the sum of the force vectors over the control volume, \bar{v} is the velocity vector, ρ is the water density, p is the pressure, \hat{n} is the unit outward normal to the control volume, and $\bar{\tau}$ is the stress tensor. For a statistically steady flow, the time average of the first integral, which is the unsteady term, is zero. The second and third integrals represent the contributions from the momentum flux and pressure, respectively. To calculate the latter, the pressure field was found using virtual-boundary, omni-directional pressure integration (Charonko et al., 2010). The last integral, which includes the contribution of viscous effects, is usually eliminated by properly choosing a control surface on whose boundaries the viscous stresses and the turbulence stresses are negligible. However, we were not able to follow this procedure as the downstream airfoil was too close to either the upstream airfoil (cases with $\Delta x = 2c$) or the downstream boundary of the image (cases with $\Delta x = 6c$). To find the stress integral, we calculated the stress tensor as:

$$\tau_{ij} = \mu \left(\frac{\partial v_i}{\partial x_j} + \frac{\partial v_j}{\partial x_i} \right), \quad (4)$$

where μ is the dynamic viscosity, $i, j = 1, 2$ and the partial derivatives were numerically obtained using the second-order central difference method. After determining the forces from Eqn 3, we used Eqns 1a and 1b to obtain the DPIV-based lift and drag coefficients.

RESULTS

Lift and drag coefficients

We determined the overall lift and drag coefficients of the tandem configurations by averaging the coefficients of the two airfoils from our load cell measurements:

$$C_{\text{tandem}} = \frac{C_{\text{upstream}} + C_{\text{downstream}}}{2}, \quad (5a)$$

where C is either the lift or the drag coefficient. For each configuration, we also averaged the lift and drag coefficients of the two single airfoils having the same angles of attack using the data from Holden et al. (2014):

$$C_{\text{single}} = \frac{C_s(\alpha_u) + C_s(\alpha_d)}{2}, \quad (5b)$$

with subscript s indicating that the single model data are used. The results were compared in Fig. 3 to elucidate the effects of the tandem

arrangement on the aerodynamic performance of the airfoils. In general, the lift coefficient demonstrated more variability than the drag coefficient, and both coefficients were influenced more by the stagger than the gap. Tandem configurations with one airfoil at an angle of attack of 0 deg and the other one at 30 deg resulted in distinct lift enhancement. In one case, ($\Delta x=2c$, $\Delta y=1c$, $\alpha_u=0$ deg, $\alpha_d=30$ deg), the tandem lift coefficient showed a 200% increase with respect to the single model data, while the drag coefficient remained almost unchanged. Fig. S1 shows that the effects of the

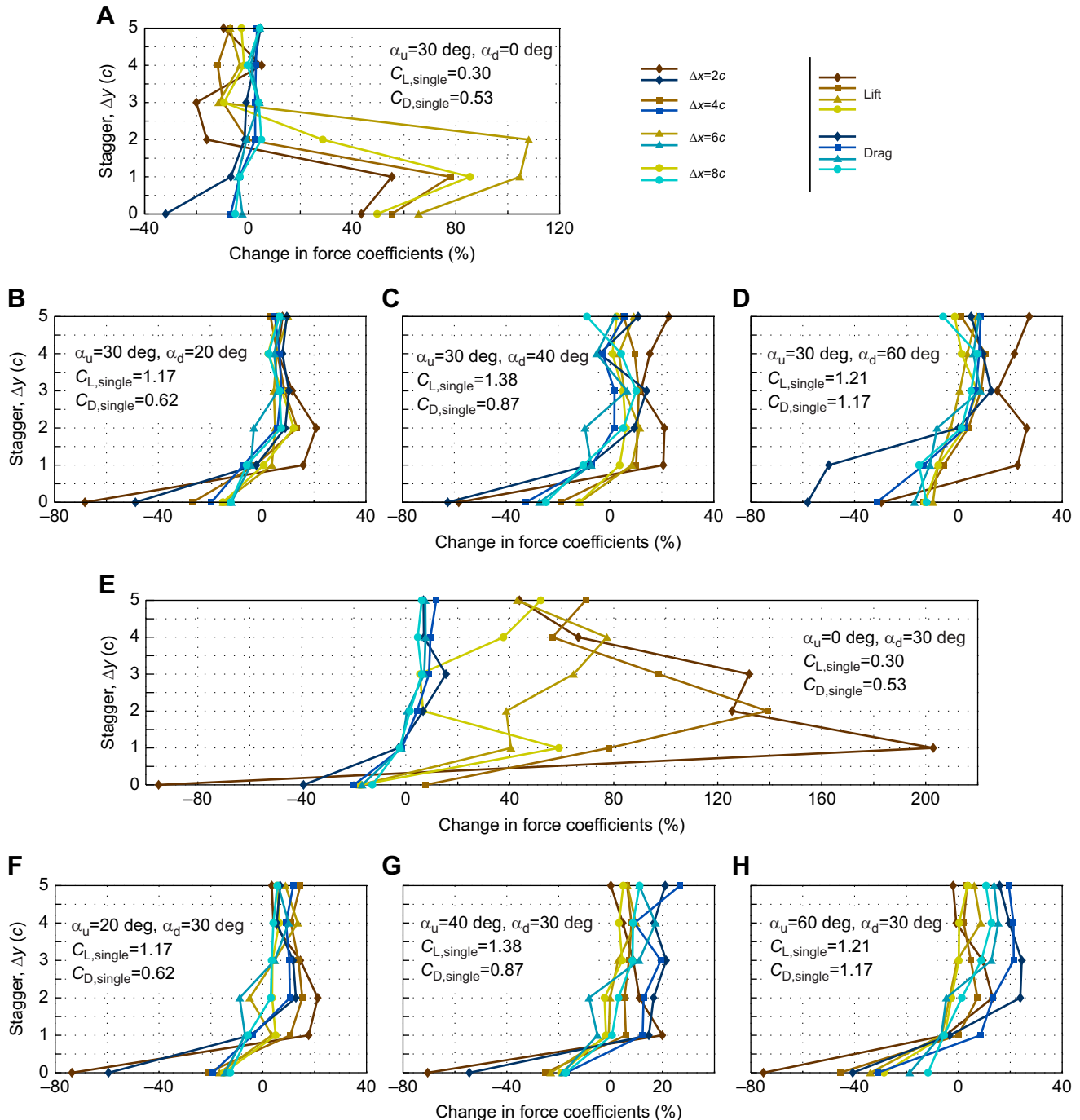


Fig. 3. The combined lift and drag measured by the load cells for the tandem system. (A–H) Data for the combinations of upstream and downstream angles of attack, α_u and α_d (see Table 1). The curves show the percentage change in the data compared with the results for single airfoils having the same angles of attack. The cases grouped in each panel have the same combination of angles of attack, and the curves depict the effects of gap (Δx) and stagger (Δy) within each group, revealing that stagger generally has a much stronger effect on the combined aerodynamic performance, and that lift is influenced by the tandem arrangement more noticeably than drag. The lift and drag coefficients of the single-model counterparts, $C_{L,\text{single}}$ and $C_{D,\text{single}}$ (Eqns 5a and 5b) are included for comparison.

tandem arrangement on L/D generally followed the trends in the lift coefficient, most noticeably for the cases with ($\alpha_u=30$ deg, $\alpha_d=0$ deg) and ($\alpha_u=0$ deg, $\alpha_d=30$ deg). An exception was the configuration with ($\Delta x=2c$, $\alpha_u=30$ deg, $\alpha_d=60$ deg), in which the significant increase in the tandem L/D resulted from simultaneous lift enhancement and drag reduction.

Contour plots of the overall L/D of the tandem airfoils in the Δx – Δy plane show that when ($\alpha_u=20$ deg, $\alpha_d=30$ deg) or vice versa, the tandem L/D was generally larger than other combinations of the angles of attack, and it was fairly insensitive to the relative position of the airfoils (Fig. 4C,D). At these combinations of angles of attack, the maximum value of the tandem L/D exceeded 2.2 and was almost

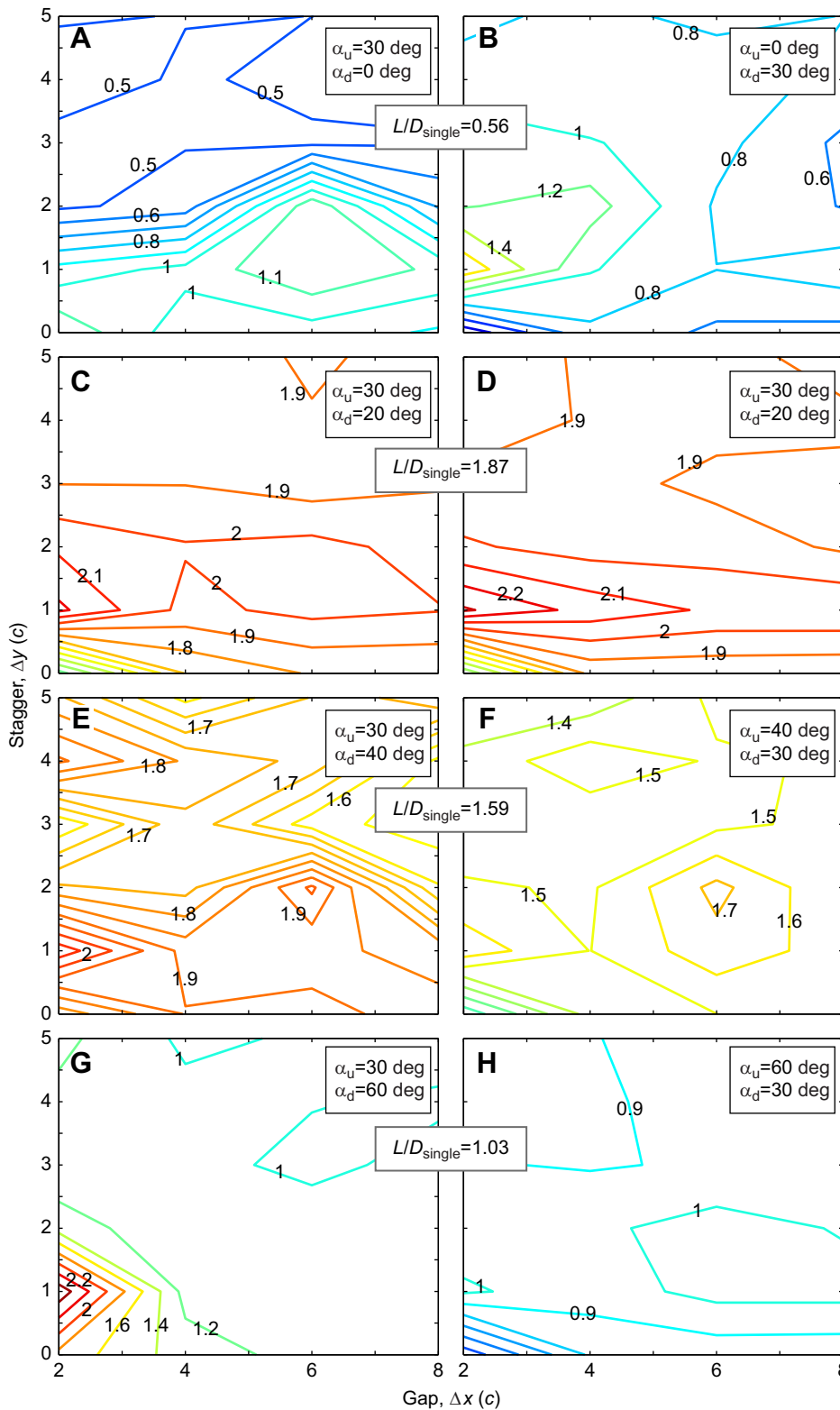


Fig. 4. Contour plots of the overall lift-to-drag ratio of the tandem airfoils in the Δx – Δy plane. (A–H) Data for the combinations of upstream and downstream angles of attack, α_u and α_d . The lift-to-drag ratio of the single-model counterparts, L/D_{single} (calculated using Eqns 5a and 5b), is included for comparison.

10% larger than the maximum lift-to-drag ratio of a single airfoil ($L/D=2$ at $\alpha=0$ deg) and 16% larger than L/D_{single} (the average of the lift-to-drag ratios of single models with the same angles of attack, found using Eqns 5a and 5b). With the other combinations of the angles of attack, the tandem configuration generally had a positive effect; however, the maximal L/D , if present, was confined to a few specific postures (e.g. the case with $\alpha_u=30$ deg, $\alpha_d=60$ deg; Fig. 4G). We also observed some negative effects; for example, a 12% decrease compared to L/D_{single} with ($\alpha_u=60$ deg, $\alpha_d=30$ deg) (Fig. 4H).

To investigate the physics underlying the aerodynamic properties of the tandem model, DPIV flow field data were collected for a select few configurations. As indicated in Fig. S1 by circled data points, the DPIV configurations included those showing significant changes in the tandem L/D with respect to single airfoil data along with some of their 'adjacent' positions without a large tandem effect. For instance, by just changing the downstream angle of attack, the significant tandem effect in one configuration ($\Delta x=6c$, $\Delta y=2c$, $\alpha_u=30$ deg, $\alpha_d=0$ deg) nearly vanished with $\alpha_d=20$ deg. In addition to visualizing the flow dynamics, DPIV data were used for calculating the lift and drag coefficients of each airfoil in order to verify those obtained from the load cell data. Fig. S2 shows that, in general, the results obtained from the two methods agreed well, with the DPIV results mostly lying within the 95% confidence interval of the load cell data, and with the maximum relative error being about 18%.

The two important subsets in the DPIV configurations were: (i) the biologically relevant cases – with ($\alpha_u=30$ deg, $\alpha_d=0$ deg), the largest increase in L/D was observed at 6 chords ($6c$) of gap and 1 to 2 chords ($1-2c$) of stagger, intriguingly coincident with the most probable relative position of the fore and the aft body in airborne snakes (Socha et al., 2010); and (ii) the extreme tandem effect cases – with ($\alpha_u=30$ deg, $\alpha_d=0$ deg), and two chords ($2c$) of gap, only one chord of change in stagger from $\Delta y=0c$ to $1c$ caused by far the biggest change in the lift-to-drag ratio. Table 2 summarizes the individual lift and drag coefficients of the two airfoils for these two groups of configurations. Within each group, the upstream and downstream angles of attack and the gap were the same, but the stagger varied. For the biologically relevant group, the upstream airfoil (30 deg angle of attack) showed similar aerodynamic performance to a single model at 30 deg angle of attack. By contrast, the downstream airfoil produced substantially larger lift and smaller drag with $\Delta y \leq 2c$; however, the enhanced performance was lost at $\Delta y=3c$. For the extreme tandem effect group, at $\Delta y=0c$, the lift

and drag of both models changed with respect to their single model counterparts, and the overall lift nearly summed to zero, resulting in a drastic negative change in the combined lift and combined L/D (Fig. 3; Fig. S1). At $\Delta y=1c$, the upstream airfoil with 0 deg angle of attack produced positive lift, as opposed to the negative lift of a single model, making the most important contribution to the drastic enhancement of the aerodynamic performance. At $\Delta y=2c$, the upstream lift became negative again but remained larger than the single model lift; therefore, the tandem system experienced a smaller positive change in aerodynamic performance.

Spectral analysis

The vortex shedding behavior of the tandem airfoils was observed from the temporal spectra of the load cell measured forces. Fig. 5A,B shows the data for the biologically relevant configurations and a few of their adjacent configurations with no significant tandem effects. The upstream airfoils, all of which had an angle of attack of 30 deg, showed power spectral densities quite similar to that of a single airfoil at the same angle of attack (Holden et al., 2014) with a distinct dominant frequency at $f^* \approx 0.23$. However, the behavior of the downstream airfoils varied with the tandem configuration. For the only two configurations with significant tandem effects ($\Delta x=6c$, $\Delta y=1c, 2c$, $\alpha_u=30$ deg, $\alpha_d=0$ deg), the downstream airfoil deviated from its single model counterpart to be 'locked' to the upstream dominant frequency. The proximity of the upstream and downstream peak frequencies for ($\Delta x=6c$, $\Delta y=2c$, $\alpha_u=30$ deg, $\alpha_d=20$ deg) could not be interpreted in the same way because the peak frequencies of single airfoils at 20 deg and 30 deg angles of attack were already close to each other. In the cases ($\Delta x=4c, 6c$, $\Delta y=3c$, $\alpha_u=30$ deg, $\alpha_d=0$ deg), the tandem arrangement had negligible influence on the downstream dominant frequency ($f^* \approx 0.34$), which remained close to that of a single airfoil. For the last configuration ($\Delta x=4c$, $\Delta y=2c$, $\alpha_u=30$ deg, $\alpha_d=0$ deg), the downstream power spectral density exhibited both previously observed peak frequencies, which indicated some influence from the upstream wake without the vortex shedding frequencies being completely locked. The temporal spectra of the extreme tandem effect cases and their adjacent configurations (Fig. 5C,D) were less orderly, with the peak frequency varying from $f^* \approx 0.23$ to $f^* \approx 0.42$, and neither of the upstream and downstream groups showed a preferred dominant frequency. In particular, no clear peak could be identified for the case ($\Delta x=2c$, $\Delta y=0c$, $\alpha_u=0$ deg, $\alpha_d=30$ deg); however, increasing the stagger to $\Delta y=1c$ resulted in two locked dominant frequencies. When the stagger was increased to $\Delta y=2c$, the secondary peak vanished and

Table 2. The individual lift and drag coefficients from the load cell measurements for the most important cases of tandem effects

		Upstream		Downstream	
		C _L	C _D	C _L	C _D
(Δx, Δy, α _u , α _d)					
Biologically relevant		α _u =30 deg		α _d =0 deg	
	(6c, 1c, 30 deg, 0 deg)	1.34±0.17	0.68±0.07	−0.11±0.02	0.34±0.04
	(6c, 2c, 30 deg, 0 deg)	1.40±0.18	0.70±0.07	−0.15±0.02	0.36±0.04
	(6c, 3c, 30 deg, 0 deg)	1.36±0.17	0.70±0.07	−0.83±0.09	0.41±0.05
Extreme tandem effects		α _u =0 deg		α _d =30 deg	
	(2c, 0c, 0 deg, 30 deg)	−0.50±0.05	0.32±0.04	0.54±0.06	0.33±0.04
	(2c, 1c, 0 deg, 30 deg)	0.19±0.02	0.49±0.05	1.63±0.18	0.55±0.06
	(2c, 2c, 0 deg, 30 deg)	−0.35±0.04	0.47±0.05	1.70±0.19	0.67±0.07
Single model data		C _L (30 deg)	C _D (30 deg)	C _L (0 deg)	C _D (0 deg)
		1.34±0.04	0.68±0.02	−0.75±0.03	0.39±0.01

The first three cases were relevant to the actual kinematics of flying snakes, and the next three cases received the largest changes in the aerodynamic performance. Within each group, the cases differ only by the stagger. The single model data (for comparison) are reported from Holden et al. (2014). C_L , lift coefficient; C_D , drag coefficient.

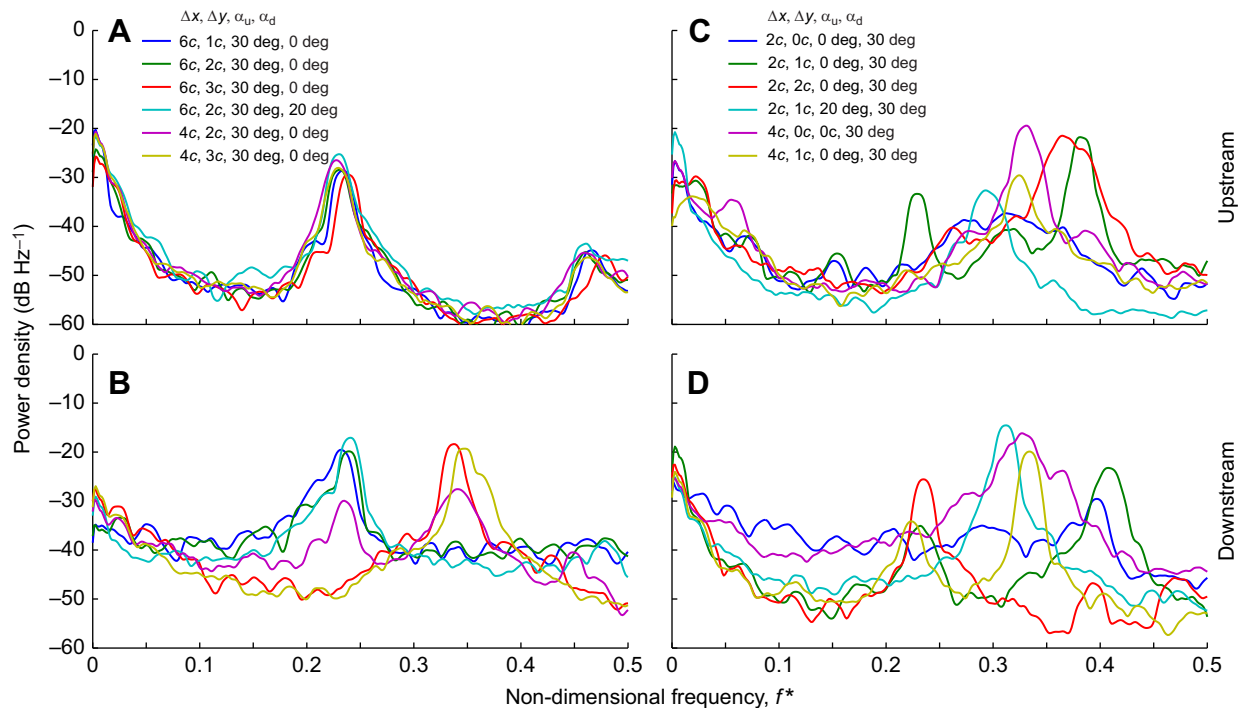


Fig. 5. Power spectral density of the force measurements showing the vortex shedding behavior of the two configuration groups of interest. (A) The upstream power spectral density (PSD) of the group related to the snake kinematics is independent of the configuration. (B) The downstream peak frequency is congruent (and potentially locked) at the upstream peak for some cases, but it is different for others. (C) The upstream PSD of the group experiencing the largest tandem effects is a function of the tandem arrangement. (D) Both of the two peak frequencies of the case with the largest lift-to-drag enhancement ($\Delta x=2c$, $\Delta y=1c$, $\alpha_u=0$ deg, $\alpha_d=30$ deg) coincide, whereas other cases exhibit less coherence between the upstream and downstream PSDs.

the primary dominant frequencies no longer matched. For all other configurations, no secondary peak was observed, but the upstream and downstream primary peaks matched.

Similar spectral behavior was observed from the spatially resolved power spectra of the vertical velocity component one chord downstream of each airfoil (Figs S3 and S4). In addition to the dominant frequencies, the velocity spectra revealed the behavior of the wake structure behind each model, indicating that the position and distribution of the wake varied with the configuration. For the biologically relevant cases (Fig. S3), the upstream high-power band was relatively narrow and symmetric relative to the airfoil position, with the maximum energy contained between $y=-c$ and $y=c$. In contrast, the downstream wake was asymmetric and shifted upward, except for the ($\Delta x=6c$, $\Delta y=2c$, $\alpha_u=30$ deg, $\alpha_d=20$ deg) case, which had a symmetric spectrum. The extreme tandem effect cases (Fig. S4) showed a strong influence of the tandem configuration on the vertical position, distribution width and frequency of the high-power band. For the case ($\Delta x=2c$, $\Delta y=0c$, $\alpha_u=0$ deg, $\alpha_d=30$ deg), the power was spread over a large range of frequencies and no dominant frequency could be identified. By increasing the stagger to $\Delta y=1c$, a clear upstream band emerged at $f^*\approx 0.42$, which was also observed in the downstream spectra at $y=2c$. In addition, the downstream spectra showed a distinct band at $f^*\approx 0.23$ that was shifted downward. Increasing the stagger to $\Delta y=2c$ caused the downstream band to become stronger and symmetric, with no trace of the upstream dominant frequency.

Fig. 6 shows the probability density of the upstream and downstream dominant frequencies for different combinations of the angles of attack. Each probability density curve was obtained from the compilation of all peaks in the spectra of any combination

of gap and stagger. The curves show that the upstream model experienced a single peak, which was always close to $f^*\approx 0.23$ when the upstream airfoil had an angle of attack of 30 deg; otherwise, it was a function of the configuration and varied with the angle of attack. The upstream dominant frequency was generally shared by the downstream model, which exhibited one or more additional peaks that could be smaller or larger than the upstream peak frequency. All in all, the tandem configuration influenced the spectra of the models by changing the dominant frequency, which was usually shared by both models, and by creating multiple peak frequencies for the downstream model.

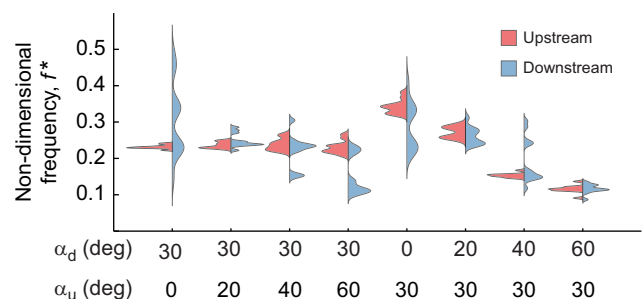


Fig. 6. Dependence of the PSD peaks on the tandem configuration. For each set of angles of attack, the probability density of the compilation of all peak frequencies of all combinations of gap and stagger was calculated and plotted separately for the upstream and downstream models. The results show that the tandem configuration could influence the spectra of the models by changing the dominant frequency, which is usually shared by both models, and by creating additional peaks for the downstream model.

Velocity fields

The velocity fields obtained from the DPIV were used to visualize the flow topology and better understand the mechanisms through which the tandem configuration modified the aerodynamic performance of the system. Fig. S5 shows the mean velocity fields for the extreme tandem effect cases of Table 2. The background color indicates the velocity magnitude normalized with respect to the freestream velocity and the gray shaded regions indicate where the flow field data could not be captured because of the shadows in the laser sheet. With zero stagger, the downstream airfoil interfered with formation of the upstream wake and caused it to become excessively elongate, a feature that was not observed with $\Delta y=1c$ or $2c$. Furthermore, the mean flow speeds in the vicinity of both airfoils were altered by the change in the stagger. For instance, the flow speed close to the dorsal surface of the downstream model at $\Delta y=0c$ was notably smaller than that at $\Delta y=1c$ or $2c$, whereas the flow speed close to the ventral surface of the upstream body decreased when the stagger was increased from $\Delta y=0c$ to $1c$.

For the configurations included in Table 2, the lift of the 0 deg angle-of-attack airfoils showed the strongest dependence on the tandem arrangement. The details of the flow structure around those airfoils were considered using the mean streamlines in their vicinity (Fig. 7). It was revealed that flow generally separated from the concave ventral surface, creating a 'trapped' vortex in the cavity. A similar behavior has been previously observed with a single snake-like airfoil at 0 deg angle of attack, for which the low pressure region created by the flow separation from the lower surface of the model dominated the dorsal wake and a negative lift was produced (Holden et al., 2014). However, with the tandem arrangement, the size of the dorsal wake and the strength of the trapped vortex varied with the configuration. In particular, for $(\Delta x=2c, \Delta y=1c, \alpha_u=0 \text{ deg},$

$\alpha_d=30 \text{ deg})$, the gap flow did not allow separation from the lower surface, and no ventral vortex could be formed (Fig. 7E).

Finally, the POD modes of the velocity field in each configuration were used to study the vortex structure in the flow. Santa Cruz et al. (2005) and Epps and Techet (2010) have shown that the first two modes can be used to accurately reconstruct the dynamics of von Kármán vortex streets. Furthermore, another index of the complexity and order of the spatio-temporal velocity field could be obtained by calculating 'entropy' from the energies of the POD modes (Santa Cruz et al., 2005). Entropy ranges from 0 to 1, with a small value indicating that most of the energy is contained in just a few modes (an ordered flow), and a large value indicating that the energy is distributed among several modes (a complex flow). Fig. S6 shows the entropies for the tandem configurations of Table 2. The majority of the tandem model entropies were larger than the maximum entropy of $H=0.425$ for a single model (Holden et al., 2014), meaning that the tandem model flow was less ordered and entailed greater turbulence. Also, the largest entropies belonged to the cases with the largest interaction between the two airfoils. In particular, a very large entropy for the case $(\Delta x=2c, \Delta y=0c, \alpha_u=0 \text{ deg}, \alpha_d=30 \text{ deg})$ was observed because the downstream airfoil interfered with the formation of upstream wake, which in return altered the flow around the downstream model. This is evident from Fig. 8A,B in which a strong and organized von Kármán vortex street could not be formed. With $\Delta y=1c$, the entropy decreased but the interaction between the models still existed as the vortices shed from the two models were coupled (Fig. 8C,D). With $\Delta y=2c$, the entropy decreased even more as the interaction between the two models considerably diminished, and the more energetic vortex shedding mode produced by the downstream model was only slightly influenced by the presence of the upstream model (Fig. 8E,F).

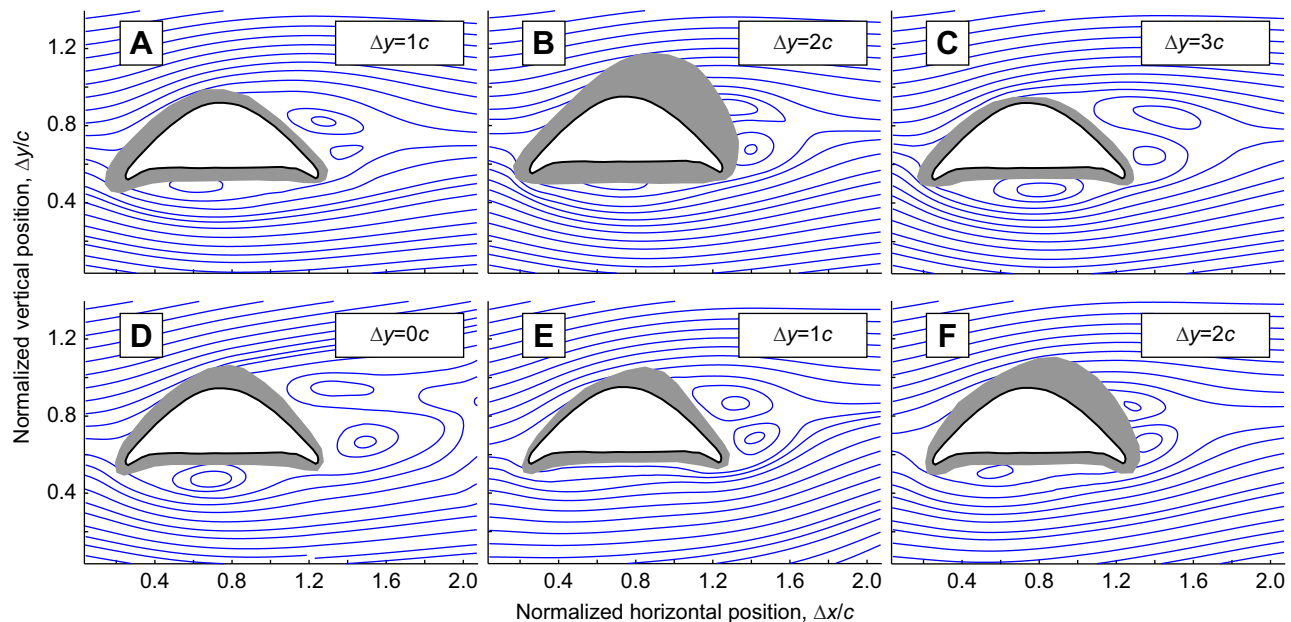


Fig. 7. Mean streamlines for cases of interest in Table 2. (A–C) The mean streamlines in the vicinity of the downstream models for the three biologically relevant cases. The configurations were the same ($\Delta x=6c, \alpha_u=30 \text{ deg}, \alpha_d=0 \text{ deg}$) except for the stagger (indicated in each panel). The vortex under the models is created when the flow on the ventral surface separates at the leading edge. The trapped vortex creates a downforce that results in negative lift. For the cases shown here, the strength of the vortex, and therefore the magnitude of the negative lift, varies with the stagger. (D–F) The mean streamlines in the vicinity of the upstream models for the three cases of extreme tandem effects. The configurations were the same ($\Delta x=2c, \alpha_u=0 \text{ deg}, \alpha_d=30 \text{ deg}$) except for the stagger (indicated in each panel), which resulted in different flow structures. In particular, with one chord of stagger, the vortex that is otherwise trapped under the model vanishes and a positive lift is achieved (see Table 2).

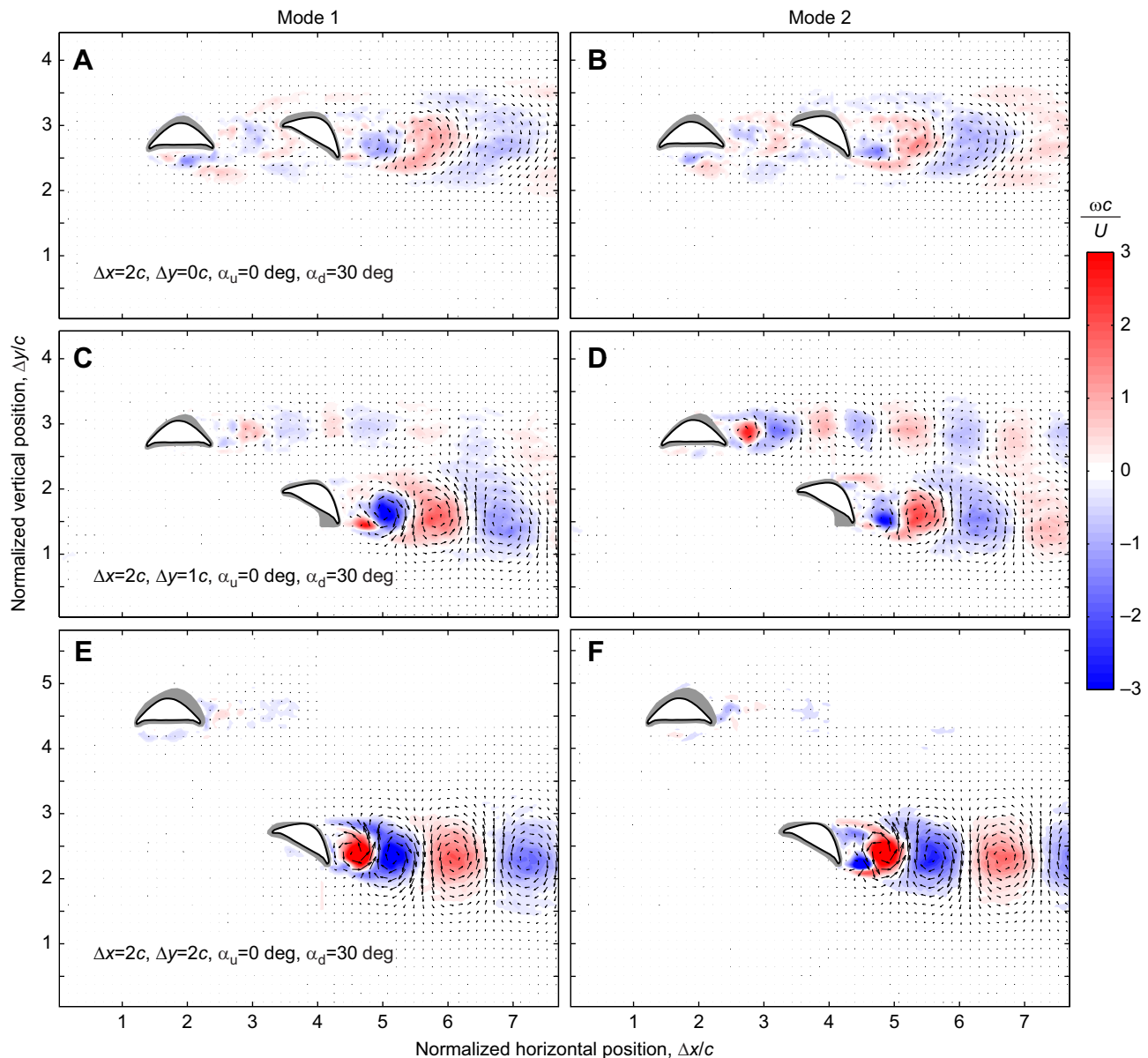


Fig. 8. The first two proper orthogonal decomposition (POD) eigenmodes for the three cases of extreme tandem effects in Table 2, illustrated by the velocity vectors and the vorticity, ω , non-dimensionalized. The panels show the eigenmodes for gap and stagger values of (A,B) $\Delta x=2c$ and $\Delta y=0c$, (C,D) $\Delta x=2c$ and $\Delta y=1c$, and (E,F) $\Delta x=2c$ and $\Delta y=2c$; the angles of attack were the same in all cases ($\alpha_u=0$ deg, $\alpha_d=30$ deg). These eigenmodes were determined from the time-resolved velocity field and represent the dynamics of von Kármán vortex streets.

DISCUSSION

Tandem aerodynamic performance

Our results showed that the tandem configuration of snake-like airfoils could produce both positive and negative aerodynamic interactions, depending on the arrangement. At best, an almost 10% enhancement of the lift-to-drag ratio can be achieved: a maximum of 2.2 for the tandem airfoils (Fig. 4) compared with a maximum of 2.0 for the single airfoil, excluding the special case of $\alpha=35$ deg (Holden et al., 2014). In the other direction, the tandem lift-to-drag ratio could be 12% smaller than L/D_{single} . The results also indicated strong dependence of aerodynamic performance of the tandem snake-like airfoils on their relative position as well as their angles of attack (Fig. 3). In general, the results were more sensitive to stagger, and the tandem effects almost universally diminished when the stagger was larger than three chord lengths. This could be explained, for the most part, by the vortex-blade interaction (interaction of vortical unsteady

flows with solid bodies; e.g. Rockwell, 1998), which was the main mechanism of aerodynamic force production in this system. With smaller stagger, the vortices shed from the upstream airfoil passed closer to the downstream airfoil, and therefore could produce a larger influence on it. This mechanism, however, could not explain the few cases for which the tandem effects increased beyond three chord lengths of stagger.

Flow field data helped to elucidate the details of how the lift and drag coefficients varied with the tandem configuration. Here, we focused on the cases with the extreme tandem effects (Fig. S5). The mean velocity fields showed that for $\Delta y=0c$, the interference of the downstream airfoil with the upstream wake resulted in a distorted wake. Moreover, the mean velocities close to the dorsal surface of the downstream airfoil did not reach the large magnitudes observed for $\Delta y=1c$ and $2c$. Therefore, the circulation-based downstream lift was considerably smaller. However, adding one chord of stagger

modified the gap flow such that: (1) the upstream wake could form but was pushed by the gap flow closer to the model, (2) the mean velocity close to the ventral surface of the upstream airfoil decreased, and (3) the mean velocity close to the dorsal surface of the downstream airfoil increased. These mechanisms augmented both the upstream and downstream lift through vortex–blade interaction and circulation modification. Increasing the stagger to $\Delta y=2c$ diminished the effects of the abovementioned mechanisms, and the combined lift and combined L/D decreased. Nonetheless, the downstream lift was a maximum at $\Delta y=2c$ because the mean wake vortices were formed closest to the dorsal surface of the downstream airfoil (Fig. 7F; and also deduced from the smaller downstream wake in Fig. S5C).

The 0 deg angle-of-attack airfoils were particularly examined because their lift production was dominated by the separation of flow from the model's lower surface originating from the leading edge. Holden et al. (2014) observed negative lift for a single airfoil at 0 deg angle of attack and argued that it was the result of a low-pressure zone on the concave ventral surface created by a vortex trapped in the cavity. In this study, the negative lift was observed for almost all of the 0 deg angle-of-attack airfoils, but the magnitude of the negative lift was dependent on the tandem configuration. The most important cases were considered in Table 2 and Fig. 7. As shown by Fig. 7A, separation occurred at the leading edge and the resulting vortex created a strong downforce that resulted in negative lift. By increasing the stagger, the trapped vortex gained more strength (Fig. 7B,C) and created larger downforces, which explains why the magnitude of the negative downstream lift increased with stagger for these cases. Fig. 7D suggests the same negative lift mechanism; however, when the stagger was increased to $\Delta y=1c$, the gap flow changed in a way that did not allow the trapped vortex to form below the airfoil (Fig. 7E). As a result, no downforce was created and the upstream lift became positive. Further increasing the stagger to $\Delta y=2c$ allowed a weak vortex to reappear (Fig. 7F), and the upstream lift became negative again, although with a smaller magnitude than the case with $\Delta y=0c$.

The vortex–blade interaction was also confirmed as the primary factor in the lift production of the tandem system by the spectral analysis results, which showed that the upstream and downstream dominant frequencies were similar for the configurations with significant effect on the lift coefficients. For instance, in Fig. 5A, the dominant frequency of the upstream airfoils (30 deg angle of attack) matched that of a single model with the same angle of attack, likely because the upstream flow was not influenced by the downstream model. The dominant frequency of the downstream airfoil (0 deg angle of attack) with $\Delta y=1c$ and $2c$ matched that of the upstream airfoil ($f^*\approx 0.23$), and a substantial lift enhancement was observed for these cases. However, at $\Delta y=3c$, the downstream dominant frequency became ‘unlocked’ from the upstream wake and its value suddenly changed to the single model value ($f^*\approx 0.34$). Thereby, the lift enhancement was entirely lost (Figs 4 and 8). Another key feature of the tandem wake was that it had a larger spatial distribution than a single model. For instance, the spatial distribution of the wake of the model at 0 deg angle of attack in tandem configuration could be comparable to that of a single model at 60 deg angle of attack (compare Figs S3 and S4 with the results of Holden et al., 2014).

Implications for gliding in flying snakes

Although our results show that large lift enhancement could be obtained with some tandem configurations, it is not possible to conclude that the snakes take the staggered posture to exploit such

aerodynamic enhancements. During a fully developed glide (i.e. at glide angles less than ~ 40 deg), the body of flying snakes does pass through these configurations, indicating that they experience the tandem aerodynamic effects. But the snakes also take postures corresponding to other configurations with $\Delta x>6c$ and $\Delta y>3c$ (Socha et al., 2010), for which little or no tandem effects were found. Moreover, the snakes rarely exhibit the small gaps needed for the largest tandem effects we observed. However, the configurations with both models at angles of attack between 20 deg and 30 deg produced a near-maximum lift-to-drag ratio for almost any combination of gap and stagger (Fig. 4). So, it is possible in theory for the snakes to modulate their body posture to exploit such optimal angles of attack, where they can assume vastly different body postures without losing the maximal L/D . In fact, during the shallower part of the glide, the snakes maintain a body angle of 25 deg from the glide path (Socha et al., 2010), but no further inferences could be made owing to the lack of data for the exact variation of the airfoil angle along the body.

Although we observed a 10% enhancement of the overall lift-to-drag ratio in certain tandem configurations, this effect was not sufficient to explain the smallest glide angles observed in snakes. None of the configurations, even those with the largest aerodynamic enhancements, could increase the overall L/D to the observed values of 3.1–4.3 exhibited in the extreme glide performances (Socha et al., 2005, 2010). However, the results of this study are not sufficient to reject the hypothesis, as a large portion of the parameter space remains unexplored. In particular, we did not examine the special angle of attack of 35 deg, for which a single airfoil produced narrow dominant peaks in the lift coefficient ($C_L=1.9$) and the lift-to-drag ratio ($L/D=2.7$) with more than 30% increase with respect to the neighboring values (Holden et al., 2014). It might be possible that the tandem interactions augment the peak even more and produce sufficiently large lift-to-drag ratios. Additionally, this study did not address the effects of the sweep angle or the 3D shape of the snake body, both of which may have significant effects on the aerodynamics of the snake.

Generalizing our findings to flying snakes suggests that they can achieve relatively large changes in the overall L/D with slight adjustments in their posture. Therefore, we postulate that it is possible for the snakes to use the staggered configuration to control their glide trajectory. A simple mechanism for this control strategy was described in a previous theoretical study (Jafari et al., 2014), in which the trajectory of the flying snake was restricted to remain in the longitudinal plane. In this control hypothesis, the snakes would have to actively keep their body in a favorable posture in which the sensitivity of the aerodynamic forces to tandem configuration is high. The biologically relevant cases being within this region of high sensitivity conforms to this mechanism of control, but follow-up experimental work is needed to test the hypothesis. It is also possible that sensitivities have negative implications, and that small control errors lead to large rotational failures. However, the fact that in hundreds of observed glides no snake has lost control (J.J.S., personal observation) provides some anecdotal evidence that the system is not unstable. Furthermore, a recent study (Yeaton et al., 2020) that incorporated a more accurate representation of the snake's 3D motion, body shape, mass distribution and aerodynamics demonstrated that the aerial undulatory motion functions as a control mechanism for flight stability.

Conclusions

This study determined the aerodynamic performance of a tandem system with airfoils having the cross-sectional shape of the flying

snake *C. paradisi*. As previously observed in studies with a single airfoil model, vortex shedding and flow separation dominate the aerodynamics of the tandem system. The main mechanism through which the tandem configuration modifies the overall aerodynamic performance is vortex-blade interaction. Overall, our findings provide new insight into the underlying physics of how the snake could maintain stability or maneuver in mid-air, despite the lack of specialized morphology serving as control surfaces. To test the existing hypotheses, these results should be incorporated into theoretical studies of the dynamics of flying snakes. Previous efforts (Jafari et al., 2014, 2017) have only considered the aerodynamic properties of a single, isolated airfoil, but clearly tandem interactions must be considered for a more accurate understanding of real snake gliding.

Acknowledgements

We thank Chris Williams and the DREAMS lab for fabrication of the snake model.

Competing interests

The authors declare no competing or financial interests.

Author contributions

Conceptualization: F.J., D.H., R.L., P.P.V., J.J.S.; Methodology: F.J., D.H., R.L., P.P.V., J.J.S.; Software: F.J., D.H.; Validation: F.J., D.H.; Formal analysis: F.J., D.H.; Investigation: F.J., D.H., R.L.; Resources: P.P.V., J.J.S.; Data curation: F.J., D.H., R.L.; Writing - original draft: F.J., D.H., R.L., P.P.V., J.J.S.; Supervision: P.P.V., J.J.S.; Project administration: P.P.V., J.J.S.; Funding acquisition: P.P.V., J.J.S.

Funding

Funding was provided by a National Science Foundation CAREER award (Physics of Living Systems, 1351322) to J.J.S. and grants from the Defense Advanced Research Projects Agency (DARPA W911NF1010040) and National Science Foundation (CBET 2027523) to J.J.S. and P.P.V.

Data availability

Data are available from the GitHub repository: <https://github.com/TheSochaLab/The-aerodynamics-of-flying-snake-airfoils-in-tandem-configuration>

References

- Akhtar, I., Mittal, R., Lauder, G. V. and Drucker, E. (2007). Hydrodynamics of a biologically inspired tandem flapping foil configuration. *Theor. Comput. Fluid Dyn.* **21**, 155–170. doi:10.1007/s00162-007-0045-2
- Bahman, J. W., Swartz, S. M., Riskin, D. K. and Breuer, K. S. (2013). Glide performance and aerodynamics of non-equilibrium glides in northern flying squirrels (*Glaucomys sabrinus*). *J. R. Soc. Interface* **10**, 20120794. doi:10.1098/rsif.2012.0794
- Berkooz, G., Holmes, P. and Lumley, J. L. (1993). The proper orthogonal decomposition in the analysis of turbulent flows. *Annu. Rev. Fluid Mech.* **25**, 539–575. doi:10.1146/annurev.fl.25.010193.002543
- Bomphrey, R. J., Lawson, N. J., Taylor, G. K. and Thomas, A. L. R. (2006). Application of digital particle image velocimetry to insect aerodynamics: measurement of the leading-edge vortex and near wake of a Hawkmoth. *Exp. Fluids* **40**, 546–554. doi:10.1007/s00348-005-0094-5
- Charonko, J. J., King, C. V., Smith, B. L. and Vlachos, P. P. (2010). Assessment of pressure field calculations from particle image velocimetry measurements. *Measurement Sci. Technol.* **21**, 105401. doi:10.1088/0957-0233/21/10/105401
- Dickson, W. B. and Dickinson, M. H. (2004). The effect of advance ratio on the aerodynamics of revolving wings. *J. Exp. Biol.* **207**, 4269–4281. doi:10.1242/jeb.01266
- Eckstein, A. and Vlachos, P. P. (2009a). Assessment of advanced windowing techniques for digital particle image velocimetry (DPIV). *Measurement Sci. Technol.* **20**, 075402. doi:10.1088/0957-0233/20/7/075402
- Eckstein, A. and Vlachos, P. P. (2009b). Digital particle image velocimetry (DPIV) robust phase correlation. *Measurement Sci. Technol.* **20**, 055401. doi:10.1088/0957-0233/20/5/055401
- Eckstein, A. C., Charonko, J. and Vlachos, P. (2008). Phase correlation processing for DPIV measurements. *Exp. Fluids* **45**, 485–500. doi:10.1007/s00348-008-0492-6
- Epps, B. P. and Techet, A. H. (2010). An error threshold criterion for singular value decomposition modes extracted from PIV data. *Exp. Fluids* **48**, 355–367. doi:10.1007/s00348-009-0740-4
- Gifford, A. R., Diller, T. E. and Vlachos, P. P. (2011). The physical mechanism of heat transfer augmentation in stagnating flows subject to freestream turbulence. *J. Heat Transfer* **133**, 021901. doi:10.1115/1.4002595
- Holden, D. (2011). *Flying snakes: aerodynamics of body cross-sectional shape*. MSc thesis, Virginia Tech, VA, USA.
- Holden, D., Socha, J. J., Cardwell, N. D. and Vlachos, P. P. (2014). Aerodynamics of the flying snake *Chrysopelea paradisi*: how a bluff body cross-sectional shape contributes to gliding performance. *J. Exp. Biol.* **217**, 382–394. doi:10.1242/jeb.090902
- Husain, Z., Abdullah, M. Z. and Yap, T. C. (2005). Two-dimensional analysis of tandem/staggered airfoils using computational fluid dynamics. *Int. J. Mech. Eng. Educ.* **33**, 195–207. doi:10.7227/IJME.33.3.2
- Jafari, F., Ross, S. D., Vlachos, P. P. and Socha, J. J. (2014). A theoretical analysis of pitch stability during gliding in flying snakes. *Bioinspir. Biomim.* **9**, 025014. doi:10.1088/1748-3182/9/2/025014
- Jafari, F., Tahmasian, S., Ross, S. D. and Socha, J. J. (2017). Control of gliding in a flying snake-inspired n-chain model. *Bioinspir. Biomim.* **12**, 066002. doi:10.1088/1748-3190/aa8c2f
- Krishnan, A., Socha, J. J., Vlachos, P. P. and Barba, L. A. (2014). Lift and wakes of flying snakes. *Phys. Fluids* **26**, 031901. doi:10.1063/1.4866444
- Lehmann, F.-O. (2008). When wings touch wakes: understanding locomotor force control by wake–wing interference in insect wings. *J. Exp. Biol.* **211**, 224–233. doi:10.1242/jeb.007575
- Lehmann, F.-O. (2009). Wing–wake interaction reduces power consumption in insect tandem wings. *Exp. Fluids* **46**, 765–775. doi:10.1007/s00348-008-0595-0
- Lentink, D. and Dickinson, M. H. (2009). Rotational accelerations stabilize leading edge vortices on revolving fly wings. *J. Exp. Biol.* **212**, 2705–2719. doi:10.1242/jeb.022269
- Maybury, W. J. and Lehmann, F.-O. (2004). The fluid dynamics of flight control by kinematic phase lag variation between two robotic insect wings. *J. Exp. Biol.* **207**, 4707–4726. doi:10.1242/jeb.01319
- Michelsen, W. and Mueller, T. (1987). Low Reynolds number airfoil performance subjected to wake interference from an upstream airfoil. AIAA Conference Paper, 87-2351.
- Miklasz, K., Labarbera, M., Chen, X. and Socha, J. J. (2010). Effects of body cross-sectional shape on flying snake aerodynamics. *Exp. Mech.* **50**, 1335–1348. doi:10.1007/s11340-010-9351-5
- Moon, B. R. (1999). Testing an inference of function from structure: Snake vertebrae do the twist. *J. Morphol.* **241**, 217–225. doi:10.1002/(SICI)1097-4687(199909)241:3<217::AID-JMOR4>3.0.CO;2-M
- Mujres, F. T., Johansson, L. C., Barfield, R., Wolf, M., Spedding, G. R. and Hedenström, A. (2008). Leading-edge vortex improves lift in slow-flying bats. *Science* **319**, 1250–1253. doi:10.1126/science.1153019
- Rockwell, D. (1998). Vortex-body interactions. *Annu. Rev. Fluid Mech.* **30**, 199–229. doi:10.1146/annurev.fluid.30.1.199
- Santa Cruz, A., David, L., Pêcheux, J. and Texier, A. (2005). Characterization by proper-orthogonal-decomposition of the passive controlled wake flow downstream of a half cylinder. *Exp. Fluids* **39**, 730–742. doi:10.1007/s00348-005-0006-8
- Scarano, F. (2001). Iterative image deformation methods in PIV. *Measurement Sci. Technol.* **13**, R1. doi:10.1088/0957-0233/13/1/201
- Scarano, F. and Riethmüller, M. L. (2000). Advances in iterative multigrid PIV image processing. *Exp. Fluids* **29**, S051–S060. doi:10.1007/s003480070007
- Scharpf, D. F. and Mueller, T. J. (1992). Experimental study of a low Reynolds number tandem airfoil configuration. *J. Aircr.* **29**, 231–236. doi:10.2514/3.46149
- Schrijer, F. F. J. and Scarano, F. (2008). Effect of predictor–corrector filtering on the stability and spatial resolution of iterative PIV interrogation. *Exp. Fluids* **45**, 927–941. doi:10.1007/s00348-008-0511-7
- Shyy, W., Trizila, P., Kang, C.-K. and Aono, H. (2009). Can tip vortices enhance lift of a flapping wing? *AIAA J.* **47**, 289–293. doi:10.2514/1.41732
- Smith, T. R., Moehlis, J. and Holmes, P. (2005). Low-dimensional modelling of turbulence using the proper orthogonal decomposition: a tutorial. *Nonlinear Dyn.* **41**, 275–307. doi:10.1007/s11071-005-2823-y
- Socha, J. J. (2002). Kinematics: gliding flight in the paradise tree snake. *Nature* **418**, 603–604. doi:10.1038/418603a
- Socha, J. J. (2011). Gliding flight in *Chrysopelea*: turning a snake into a wing. *Integr. Comp. Biol.* **51**, 969–982. doi:10.1093/icb/ict092
- Socha, J. J., O'dempsey, T. and Labarbera, M. (2005). A 3-D kinematic analysis of gliding in a flying snake, *Chrysopelea paradisi*. *J. Exp. Biol.* **208**, 1817–1833. doi:10.1242/jeb.01579
- Socha, J. J., Miklasz, K., Jafari, F. and Vlachos, P. P. (2010). Non-equilibrium trajectory dynamics and the kinematics of gliding in a flying snake. *Bioinspir. Biomim.* **5**, 045002. doi:10.1088/1748-3182/5/4/045002
- Socha, J. J., Jafari, F., Munk, Y. and Byrnes, G. (2015). How animals glide: from trajectory to morphology. *Can. J. Zool.* **93**, 901–924. doi:10.1139/cjz-2014-0013
- Song, J., Luo, H. and Hedrick, T. L. (2014). Three-dimensional flow and lift characteristics of a hovering ruby-throated hummingbird. *J. R. Soc. Interface* **11**, 20140541. doi:10.1098/rsif.2014.0541

- Usherwood, J. R. and Lehmann, F.-O.** (2008). Phasing of dragonfly wings can improve aerodynamic efficiency by removing swirl. *J. R. Soc. Interface* **5**, 1303–1307. doi:10.1098/rsif.2008.0124
- Vogel, S.** (2003). *Comparative Biomechanics: Life's Physical World*. Princeton, New Jersey, USA: Princeton University Press.
- Wang, Z. J. and Russell, D.** (2007). Effect of forewing and hindwing interactions on aerodynamic forces and power in hovering dragonfly flight. *Phys. Rev. Lett.* **99**, 148101. doi:10.1103/PhysRevLett.99.148101
- Wang, S., Zhang, X., He, G. and Liu, T.** (2014). Lift enhancement by dynamically changing wingspan in forward flapping flight. *Phys. Fluids* **26**, 061903. doi:10.1063/1.4884130
- Warkentin, J. and Delaurier, J.** (2007). Experimental aerodynamic study of tandem flapping membrane wings. *J. Aircr.* **44**, 1653–1661. doi:10.2514/1.28160
- Weimerskirch, H., Martin, J., Clerquin, Y., Alexandre, P. and Jiraskova, S.** (2001). Energy saving in flight formation. *Nature* **413**, 697–698. doi:10.1038/35099670
- Westerweel, J. and Scarano, F.** (2005). Universal outlier detection for PIV data. *Exp. Fluids* **39**, 1096–1100. doi:10.1007/s00348-005-0016-6
- Yeaton, I. J., Ross, S. D., Baumgardner, G. A. and Socha, J. J.** (2020). Undulation enables gliding in flying snakes. *Nat. Phys.* **16**, 974–982. doi:10.1038/s41567-020-0935-4

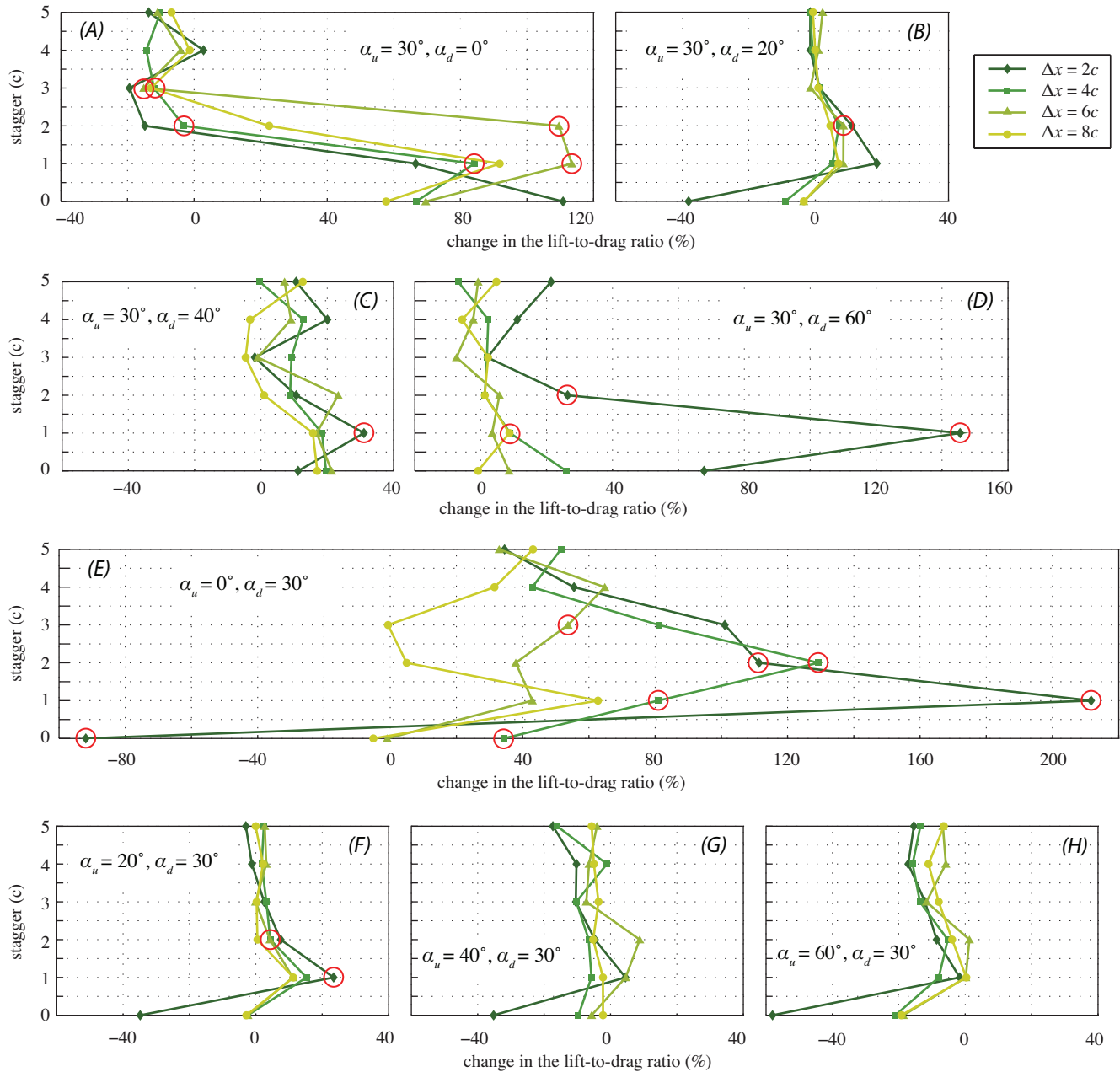


Fig. S1. The combined lift-to-drag ratio for the tandem system. The curves show the percent change in the data compared to the results for single airfoils having the same angles of attack. The cases grouped in each panel have the same combination of angles of attack. The cases with striking lift-to-drag augmentation along with their ‘neighbors’ that lack such effects were selected for the PIV experiments. The PIV cases are shown in the figure by the circled data points.

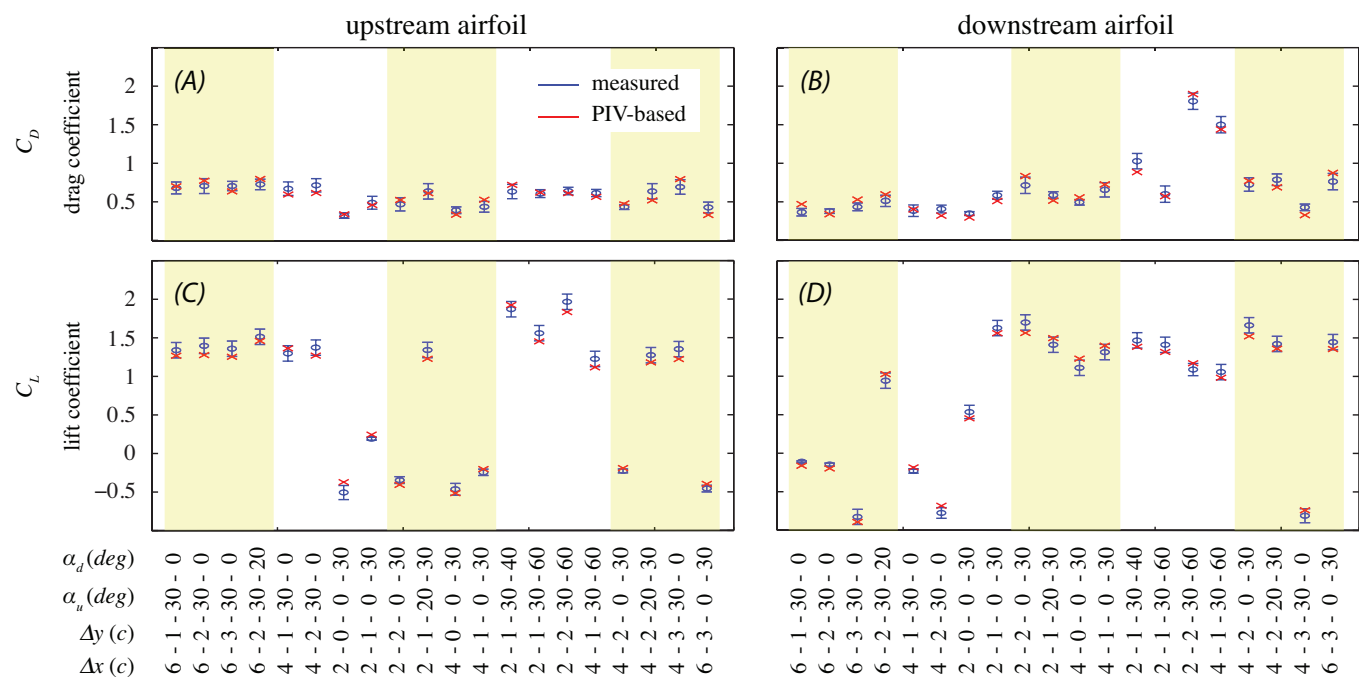


Fig. S2. Comparison between the load cell measurements and the PIV-based estimation of the lift and drag coefficients. The error bars indicate the 95% confidence intervals of the measured load cell data.

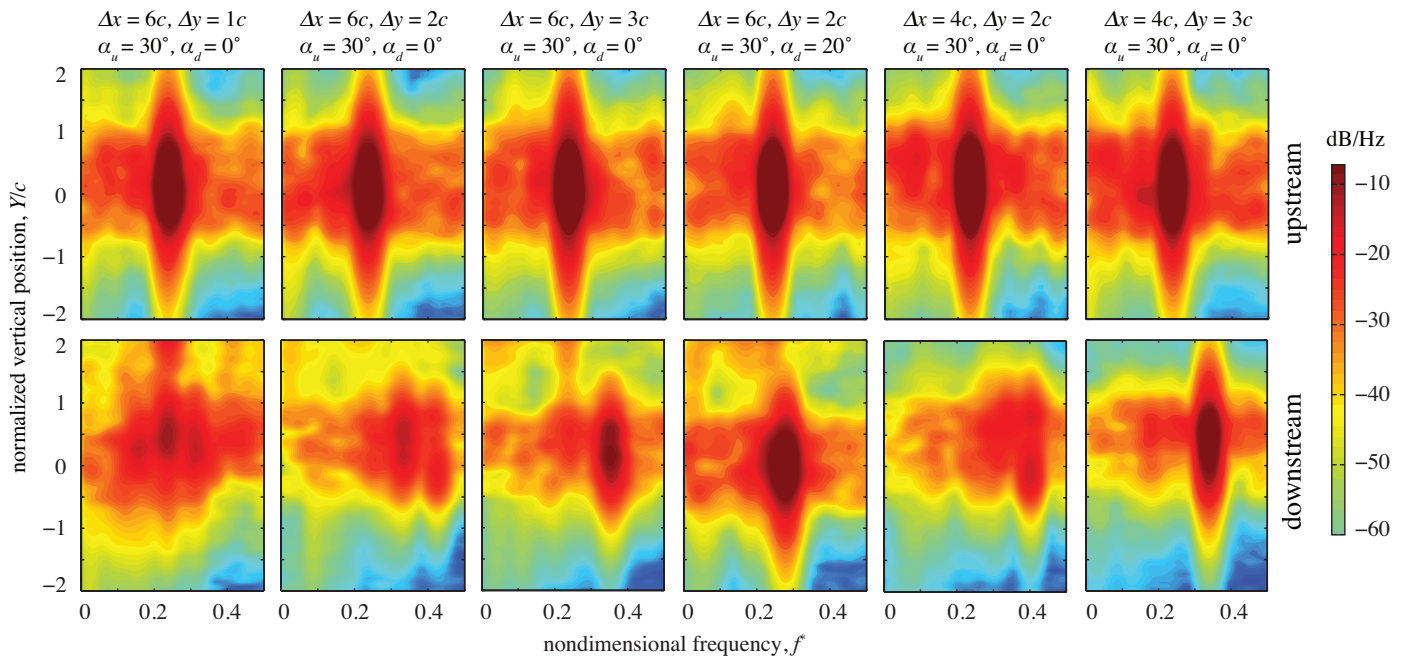


Figure S3. Spatially resolved PSD of the vertical velocity component one chord downstream of each airfoil from the tandem configurations related to the flying snake kinematics (compare with Figs. 5A and 5B). The upstream results with a single dominant frequency suggest a conventional bluff body wake. The downstream wakes are generally more turbulent and contain a broader spectrum of flow structures; however, the cases with the largest stagger ($\Delta y = 3c$) have structured wakes.

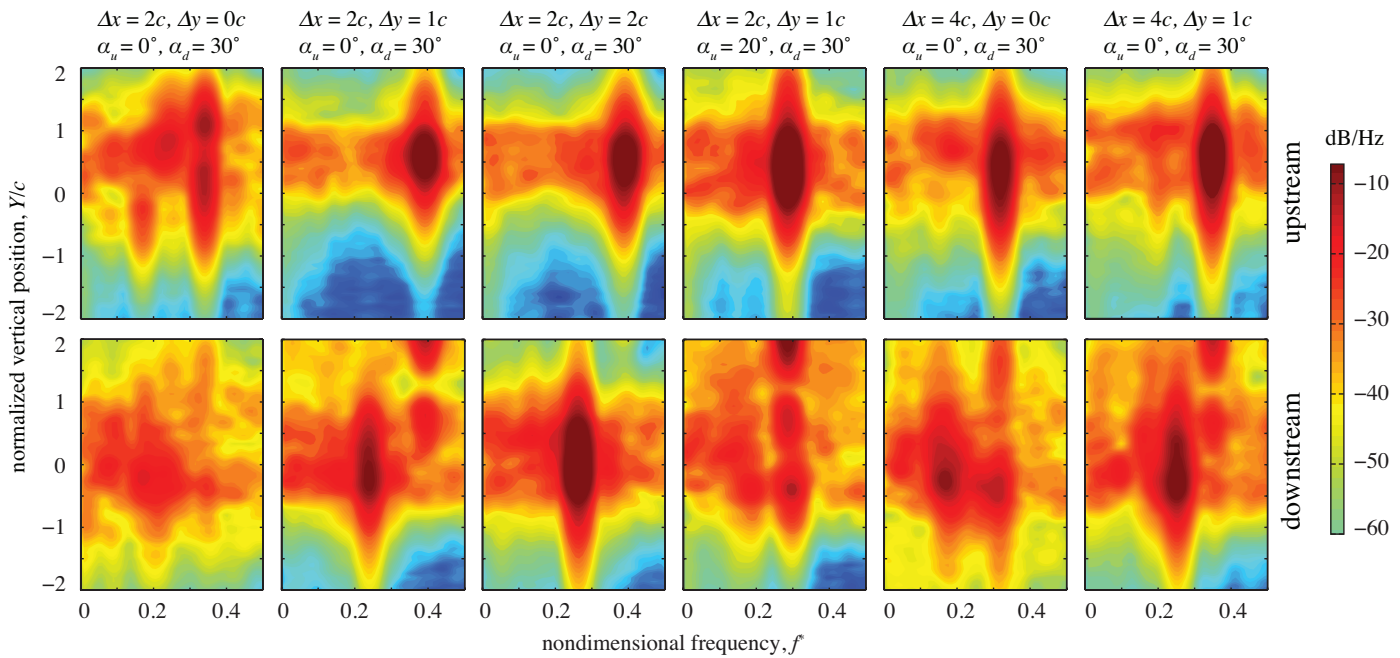


Figure S4. Spatially resolved PSD of the vertical velocity component one chord downstream of each airfoil from the configurations experiencing the largest tandem effects (compare with Figs. 5C and 5D). Except for the first configuration ($\Delta x = 2c$, $\Delta y = 0c$, $\alpha_u = 0^\circ$, $\alpha_d = 30^\circ$), the upstream wakes have a single dominant frequency, which varies with gap and stagger. The downstream wakes are generally more turbulent and the power is spread through a large range of space and frequency domain.

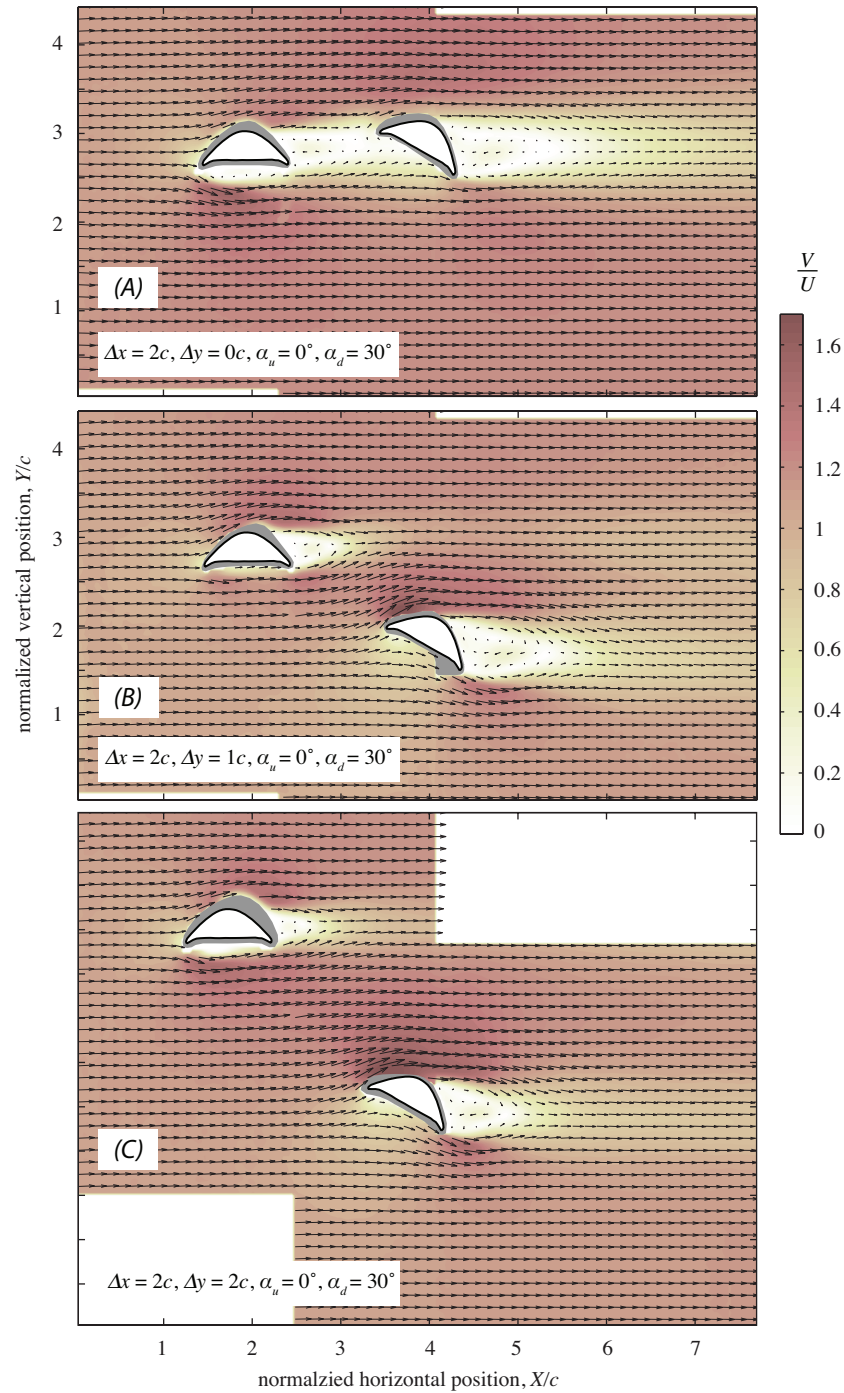


Figure S5. The mean velocity field for three of the cases experiencing the largest tandem effects (see Table 2). The background color indicates the normalized velocity magnitude, and the gray shades are the regions where the flow could not be resolved owing to shadows. The configurations are the same except for the stagger. The flow field around the upstream and downstream models are both influenced by the configuration.

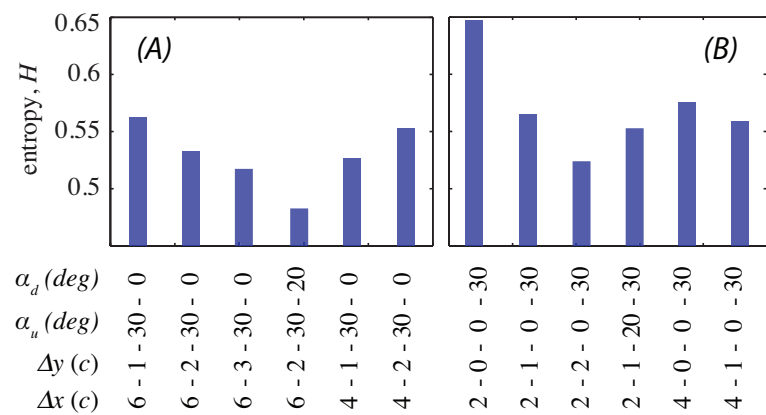


Figure S6. The entropy associated with the POD, which indicates the level of flow organization, for (A) the cases related to the kinematics of flying snakes, and (B) the cases experiencing the largest tandem effects.